Journal of Materials Chemistry B

PAPER

View Article Online
View Journal | View Issue

Cite this: J. Mater. Chem. B, 2018, 6, 1026

Magnetic lipid nanocapsules (MLNCs): self-assembled lipid-based nanoconstruct for non-invasive theranostic applications†

Vikas Nandwana,[ab] Abhalaxmi Singh,[ab] Marisa M. You,[a] Gefei Zhang,[a] John Higham,[ac] Tiffany S. Zheng,[a] Yue Li,[a] Pottumarthi V. Prasad[d] and Vinayak P. Dravid *[ab]

Received 7th December 2017,
Accepted 3rd January 2018

DOI: 10.1039/c7tb03160b

rsc.li/materials-b

We report magnetic nanostructure-stabilized lipid nanocapsules (MLNCs) that show superior structural stability and theranostic properties compared to conventional lipid-based nanocarriers. As therapeutic nanocarriers, the MLNCs exhibit a therapeutic efficacy that is 16 times greater than that of free drugs due to their high payload capacity and actuated drug release ability. In addition, the magnetic resonance contrast enhancement of the MLNCs is nine times higher than that of a clinically approved T_2 MRI contrast agent (ferumoxytol), demonstrating the diagnostic imaging capability of the MLNCs in MRI. The self-assembly method to synthesize the lipid nanocapsules is extended to other types of nanoparticles (gold nanoparticles and quantum dots) to produce lipid nanohybrids with distinct physical properties.

Lipid-based nanostructures and liposomes in particular are accepted as drug delivery carriers in clinical applications due to their excellent biocompatibility and biodegradability.[1–4] Since they are made of "natural" components, they can degrade and metabolize in the body without producing any toxicity. In addition, their ability to entrap both hydrophilic and lipophilic drugs and protect the drugs from the surrounding environment gives them an edge over other drug delivery platforms. Today, several formulations of liposomes are already approved by the FDA as therapeutic nanocarriers.[1,4,5] However, liposomes pose several challenges related to the formation process and the structural stability of the formulations.[6] Drug delivery from liposomes is based on diffusive release, which cannot be controlled. While the permeability of the lipid membrane can be tuned during synthesis to control drug release, this can compromise the structural stability of the liposome.[6] Lastly, liposomes have been largely successful as drug delivery carriers in clinical settings, without any major success in diagnostics.

Integrating inorganic nanostructures such as gold nanoparticles, quantum dots, and magnetic nanostructures with liposomes has been used as a strategy to provide stability, diagnostic ability, and stimuli-based drug release.[7–10] In particular, magnetic nanostructures (MNS) have received significant attention as non-invasive theranostic agents due to their superparamagnetic nature, ability to enhance localized contrast in magnetic resonance imaging (MRI) and thermal activation under external radio-frequency (RF) field.[11–16] Several formulations of MNS are clinically approved due to their excellent biocompatibility and biodegradability.[17–19] Although MNS as T_2 MRI contrast agents have been well established in diagnostic imaging,[20] their potential in therapy has not yet been fully explored. Due to their complementary advantages, liposome-encapsulated/embedded MNS (also called magnetoliposomes) have been suggested as an attractive option for theranostic nanocarriers.[8,21–26] However, when MNS are encapsulated in the hydrophilic cores of liposomes,[24,25] they suffer from low thermal activation efficiency due to the high thermal conductivity of water and poor MRI contrast enhancement resulting from the hydrophobic lipid bilayer.[27–31] On the other hand, when MNS are embedded in the lipid bilayer, controlling the encapsulating efficiency and distribution of the MNS in the lipid membrane is a formidable challenge.[27,32–34]

Recently, nano- and microcapsules with colloidal particle shells have attracted immense interest as delivery vehicles.[35,36] Based on this motivation, we report the synthesis of a novel MNS-stabilized lipid nanoconstruct that shows higher structural stability and enhanced theranostic ability compared to

[a] Department of Materials Science & Engineering, Northwestern University, Evanston, Illinois 60208, USA. E-mail: v-dravid@northwestern.edu
[b] International Institute of Nanotechnology, Evanston, Illinois 60208, USA
[c] Department of Biomedical Engineering, University of Notre Dame, Notre Dame, IN 46556, USA
[d] Department of Radiology, Northshore University Healthcare, Evanston, Illinois 60201, USA

† Electronic supplementary information (ESI) available: TEM of collapsed MLNCs (Fig. S1), TEM of control experiments (Fig. S2, TEM of different size MLNCs (Fig. S3 and S4), dose-dependent cellular uptake of MLNCs (Fig. S5). See DOI: 10.1039/c7tb03160b

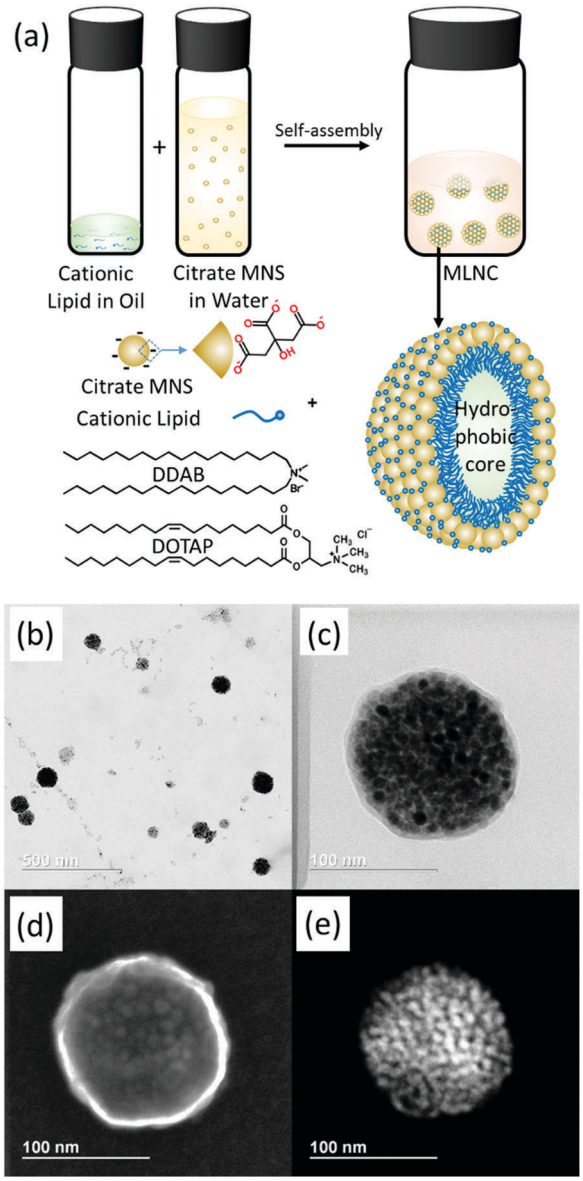

Fig. 1 (a) Formation and detailed architecture of the MLNCs. Scanning transmission electron microscopy (STEM) images of the MLNCs in (b and c) bright-field, (d) scanning, and (e) dark-field modes.

conventional MNS/lipid-based carriers. When MNS (in water) and lipids (in oil) with complementary functionalities are emulsified under particular reaction conditions, they self-assemble into MNS-stabilized lipid nanocapsules (MLNCs; Fig. 1a). The sizes of the MLNCs can be tuned from 25 to 400 nm. The structures of the MLNCs are different than those of previously reported magnetoliposomes; the MNS in the MLNCs are neither encapsulated in the core nor embedded in the lipid membrane.[23–25] Rather, the MNS are densely packed along with lipid heads on the nanocapsule surface, which does not compromise any of the physical properties of the MNS. The use of hydrophilic MNS provides advantages compared to previously reported emulsion-based nanoconstructs that use hydrophobic MNS.[37,38] The lateral crosslinking resulting from complementary interactions between the MNS and lipid heads generate MLNC surfaces with high structural stability. The hydrophobic cores of the MLNCs, which are constructed by non-polar chains of the lipid and oil, allow high loading of lipophilic drugs. In addition to stability, the presence of MNS contributes to actuated drug release (due to the thermal activation of MNS) and additional diagnostic capability (due to the enhancement of MRI contrast by MNS). Due to their unique structure, the MLNCs loaded with PTX show significantly higher therapeutic efficacy compared to free PTX and higher MRI contrast enhancement compared to conventional T_2 MRI contrast agents. Lastly, we extended the self-assembly method to fabricate nanocapsules of other types of inorganic nanoparticles (gold nanoparticles and quantum dots).

Fig. 1a shows the formation process of the MLNCs using negatively charged MNS (citrate MNS) and cationic lipids (DDAB or DOTAP). Fig. 1b–e show the STEM images of MLNCs (size = 100 nm) made from 8 nm citrate MNS and lipids. The TEM image of a crumbled nanocapsule confirms the hollow-core structure of the MLNCs (Fig. S1, ESI†). The hydrodynamic size and zeta potential are observed as ~130 nm and ~28 mV, respectively. The MLNCs show good long-term stability. Using dynamic light scattering, a stability study was done for five days in DI water, phosphate buffer saline (PBS), and cell culture media, and the hydrodynamic size and PDI value did not change significantly (Fig. S2, ESI†). No MLNC formation was observed when MNS and lipids with non-complementary functionalities were used (Fig. S3, ESI†). The sizes of the MLNCs were controlled by tuning the lipid/MNS molar ratio, and MLNCs with sizes of 25 to 450 nm were synthesized (Fig. S4 and S5, ESI†). However, 100 nm MLNCs composed of 8 nm citrate MNS were used in all diagnostic and therapeutic experiments due to their optimum size range and physical properties.

The potential to apply the MLNCs in MRI contrast enhancement was investigated by measuring the spin–spin relaxation time (T_2) of the MLNCs in 3 T MRI. The decrease in the T_2 of the MLNCs was significantly higher than that of the isolated citrate MNS that were used to form the MLNCs (Fig. 2). As a result, the r_2 relaxivity of the MLNCs (680 mM^{-1} s^{-1}) was higher than those of the citrate MNS (425 mM^{-1} s^{-1}) and the FDA-approved T_2 contrast agent ferumoxytol (81 mM^{-1} s^{-1}).[17,39–41] The higher r_2 of MLNC compared to the citrate MNS can be explained by the synergistic interactive magnetism theory reported by Gillis *et al.*[40] Nanoclusters made of magnetic nanoparticles generate a stronger magnetic moment per unit volume than isolated magnetic nanoparticles. The r_2 relaxation of magnetic nanoclusters can be expressed as[40]

$$r_2 = \left(\frac{64\pi}{135}\right)\left(\mu N_g \frac{L(x)}{4\pi}\right)^2 \frac{N_A C_a}{R_a D}, \quad (1)$$

where μ is the magnetic moment of the nanoparticle, N_g is the number of nanoparticles assembled in the cluster, C_a is the cluster concentration, R_a is the average cluster radius, D is the water diffusion coefficient, N_A is Avogadro's number, and $L(x)$ is the Langevin function. As shown in eqn (1), the stronger magnetic field surrounding clusters directly influences water

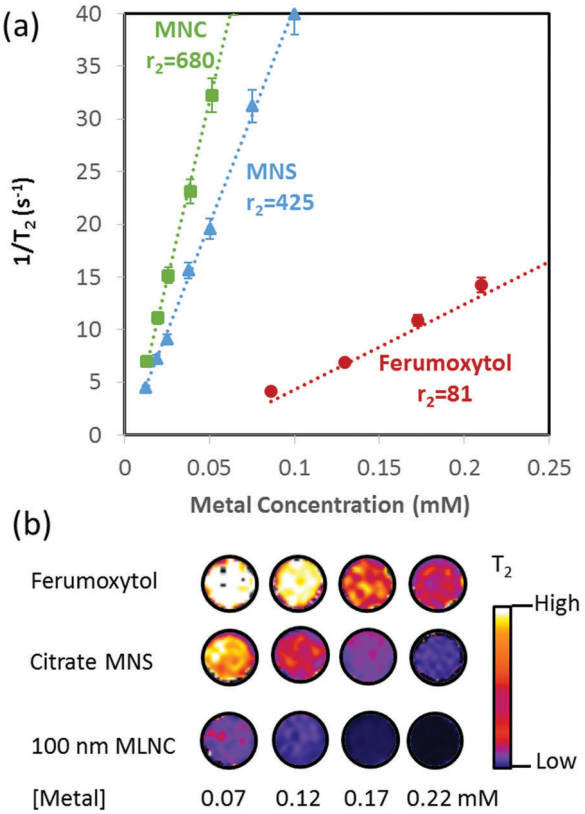

Fig. 2 (a) r_2 relaxivity plots and (b) color intensity maps of ferumoxytol, citrate MNS, and MLNCs. T_2 (spin–spin relaxation time) was measured using MRI with a field strength of 3 T.

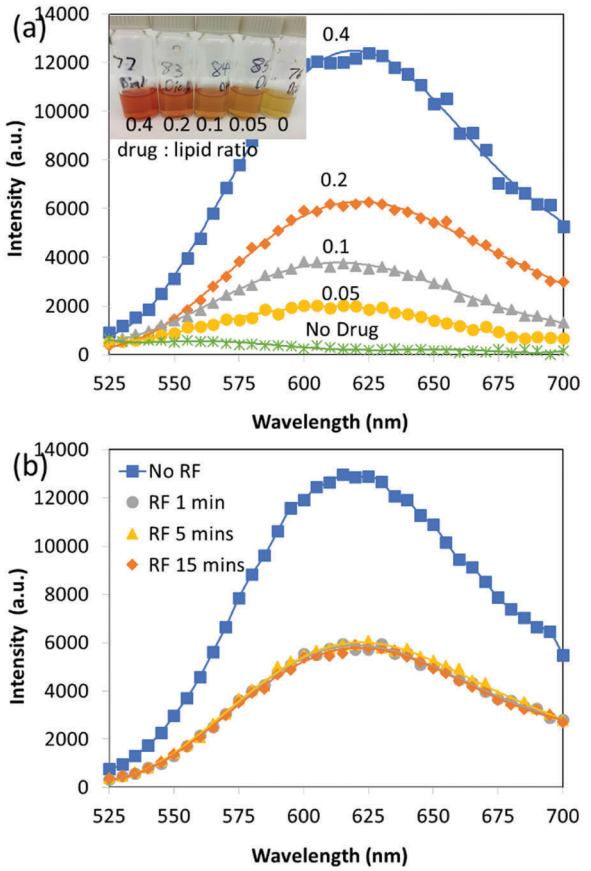

Fig. 3 (a) Fluorescence spectra and photograph (inset) of MLNCs loaded with drug : lipid ratios ranging from 0 to 0.4 (w/w), confirming that drug can be loaded in a controlled manner. (b) Time-dependent drug release study of MLNCs under RF field (5 kA m^{-1}, 300 kHz) for 1, 5, and 15 min. The decrease in fluorescence confirms the drug release, and similar fluorescence at different RF exposure times suggests that release occurs as a burst mechanism.

proton relaxation, resulting in higher relaxivity compared to isolated magnetic nanoparticles.[41–43]

The hydrophobic cores of the MLNCs allow the loading of lipophilic therapeutic cargo that can be released in a controlled manner under RF field based on the thermal activation of MNS. To demonstrate the drug encapsulation and actuated release capability of the MLNCs, the lipophilic fluorescent drug curcumin (CUR) was used (Fig. 3). Drug encapsulation was achieved by mixing the drug into a lipid solution during MLNC formation. Unencapsulated CUR was removed after dialysis and centrifugation, and the final CUR concentration in the MLNCs was calculated using the standard fluorescence CUR plot. Based on the initial and final CUR concentrations, an encapsulation efficiency greater than 80% was observed. Controlled amounts of CUR were loaded in the MNS with drug : lipid ratios (w/w) of 0.05 to 0.4. We observed a systematic increase in fluorescent intensity from low to high CUR concentration, demonstrating the successful drug encapsulation in the MLNCs and highlighting their potential to encapsulate high payloads of lipophilic drugs (Fig. 3a). The highest drug : lipid ratio (w/w) obtained in this study (0.4) is significantly higher than previously reported for CUR-loaded lipid-based drug delivery systems.[44–46] The maximum drug : lipid ratio of the MLNCs is also higher than those of various FDA-approved liposomal drug carriers (0.125 for Doxil, 0.27 for Myocet, 0.05 for Daunoxome, 0.1 for Lipoplatin, and 0.004 for Mepact).[47] It is important to note that approximately 40% of approved drugs used in clinical treatment have poor water solubility.[48] Due to their hydrophobic character, these drugs are currently administered *via* a variety of strategies such as pH modification, salt forms, and surfactant solubilization, which affects their efficacy to some extent.[48,49] Due to their high encapsulation efficiency and high payload capacity, the MLNCs offer an excellent alternative for the administration of lipophilic drugs without any modification of the drug's original structure.

Drug release in conventional drug-based carriers is based on diffusion and cannot be controlled. In most cases, controlled release at the target site is required to reach a drug concentration in the therapeutic range.[6] Actuated release is an important mechanism for drug release where drugs can be released on demand in the presence of an external stimuli.[5] Compared to stimuli such as heat, light, electric field, and ultrasound, the use of an RF field (also called alternative magnetic field at RF) is appealing due to its non-invasive nature and deep tissue penetration.[50] To demonstrate RF field-actuated drug release, CUR-loaded MLNCs with a drug : lipid ratio of 0.4 (w/w) were exposed to RF field (5 kA m^{-1}, 300 kHz) for 1, 5, and 15 min, and fluorescence was measured after the removal of released drug. A significant decrease in

fluorescence was observed after exposure to the RF field, suggesting that the thermal activation of the MLNCs resulted in the release of a substantial amount of CUR (Fig. 3b). Based on the CUR concentrations before and after RF field exposure, ~65% of the drug was released. Interestingly, time did not affect the amount of drug released; the decrease in fluorescence was similar at different time intervals, implying that the drug was released in a burst mechanism.

The cell viability and dose-dependent uptake of the MLNCs was validated in two different cell lines (J774 and HepG2; Fig. 4a and Fig. S6, ESI†), while the uptake of MLNCs in HepG2 cells was confirmed by STEM and EDS spectral scans, point scans, and elemental maps (Fig. 4b). It is important to note the structural stability of the MLNCs after cell uptake. Since the surfaces of the MLNCs are composed of MNS and/or lipid heads with complementary functionalities, complementary interactions between MNS and lipids play a decisive role in stabilizing the MLNCs. One reason for this stability is the presence of nanoparticles at the external liposome surfaces, which was reported by Granick *et al.*[7] to improve stability. This superior stability of the MLNCs allows them to maintain their spherical structures after cell uptake. To demonstrate the MLNCs' potential as a therapeutic nanocarrier, the anti-cancer drug PTX was loaded into the MLNCs and treated with HepG2 cells. Different concentrations of MLNCs with and without PTX were incubated with HepG2 cells and exposed to RF field for 15 min.

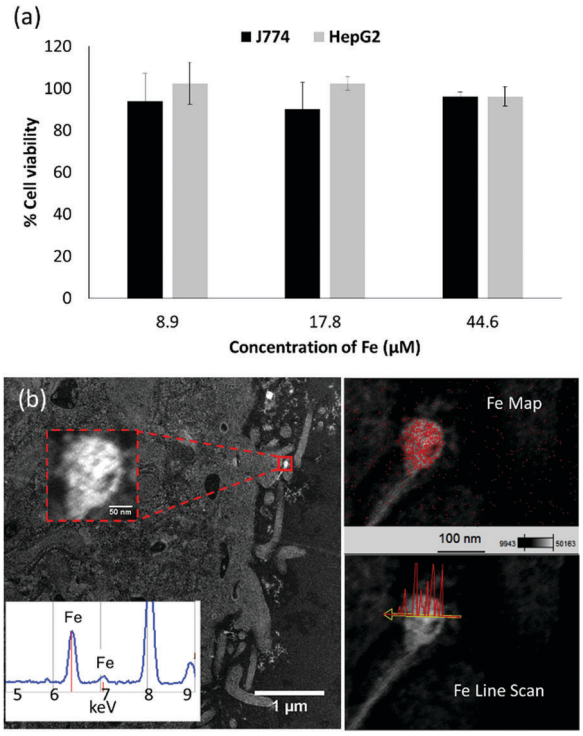

Fig. 4 (a) Cell viability study using MTS assay. J774 murine macrophage cells and HepG2 cancer cells were treated with different concentrations of MLNCs, and cell viability was assessed after 24 hours. (b) STEM image, EDS elemental map, line scan and spectral scan (inset) of Fe confirm the presence of MLNCs in HepG2 cells.

The MLNCs without PTX exhibited no cytotoxicity towards HepG2 cells (Fig. 5a). HepG2 cells treated with PTX-loaded MLNCs (MLNC-PTX) showed greater cytotoxicity than free PTX. As a result, the half maximal inhibitory concentration (IC_{50}) values of the HepG2 cells were 0.63 and 0.13 μg PTX per mL for free PTX and PTX-loaded MLNCs, respectively, suggesting that the efficacy was enhanced by five times when PTX was encapsulated within the MLNCs (Fig. 5a). The cytotoxicity of the PTX-loaded MLNCs increased in a dose-dependent manner. Cells treated with MLNCs and exposed to RF field (MLNC + RF) also induced cytotoxicity in the HepG2 cancer cells. Since exposure to RF field generates heat in the local environment of the MNS, the induced cytotoxicity is likely attributed to the higher thermal sensitivity of the cancer cells as compared to normal cells.[51] However, the combination of PTX-loaded MLNCs and RF field (MLNC-PTX + RF) resulted in the maximum cytotoxicity to HepG2 cells, with cell death reaching up to 75%. The IC_{50} value for MLNC-PTX + RF was calculated to be 0.04 μg PTX per mL, ~16 times lower than that of free PTX (0.63 μg PTX per mL) (Fig. 5b). The combination index (CI) of PTX-loaded MLNCs after exposure to RF field was 0.163, suggesting that the two kinds of therapies (chemo + thermal) are highly synergistic. The 16-fold increase in therapeutic efficacy obtained by combining the two types of therapies can be attributed to different reasons. First, the thermal activation of MNS *via* RF field facilitated the burst release of encapsulated drugs by inducing structural instability in the MLNCs. The application of RF to release encapsulated drugs was previously demonstrated by our group in an MNS-based hydrogel platform.[52] Second, the increase in the sensitivity of cancer cells to anticancer drugs after exposure to thermal therapy enhanced cytotoxicity.[51] In other experimental setups, thermal activation helped increase the effectiveness of clinically tested radiotherapy or chemotherapy in patients with different cancers, including malignant melanoma, glioblastoma, cervical cancer, and lymph node metastases.[53,54]

To demonstrate the diagnostic imaging capability of the MLNCs, T_2-weighted MRI images of MLNC-labelled HepG2 cell pallets were acquired (Fig. 5c). For Fe concentrations up to 1 μM, a significant drop in T_2 relaxation time was observed compared to ferumoxytol, demonstrating the contrast-enhancement property of the MLNCs (Fig. 5d). It is important to emphasize the correlation between therapeutic efficacy and imaging concentration of the MLNCs. As described in Fig. 4b, the minimum concentration of MLNCs (with PTX and RF) for effective therapy was 14.6 μM [Fe]. We believe that this concentration should be sufficient to generate an MRI (3 T) signal as we have observed signals from MLNCs at concentrations as low as 10 μM [Fe] in solution (Fig. 2e) and 1 μM [Fe] in cell pellets (Fig. 4d). In contrast, no signal was observed from ferumoxytol at a similar [Fe].

Nanocapsule formation was extended to other nanoparticles of different types/sizes, resulting in lipid nanocapsules with distinct physical properties. Fig. 6a–d show TEM images and EDX spectra of magnetic, plasmonic, and semiconducting lipid nanocapsules of different sizes assembled from 4 and 8 nm MNS, 13 nm Au NPs, and 6 nm CdSe/ZnS QDs. The absorbance and fluorescence plots of plasmonic and semiconducting nanocapsules

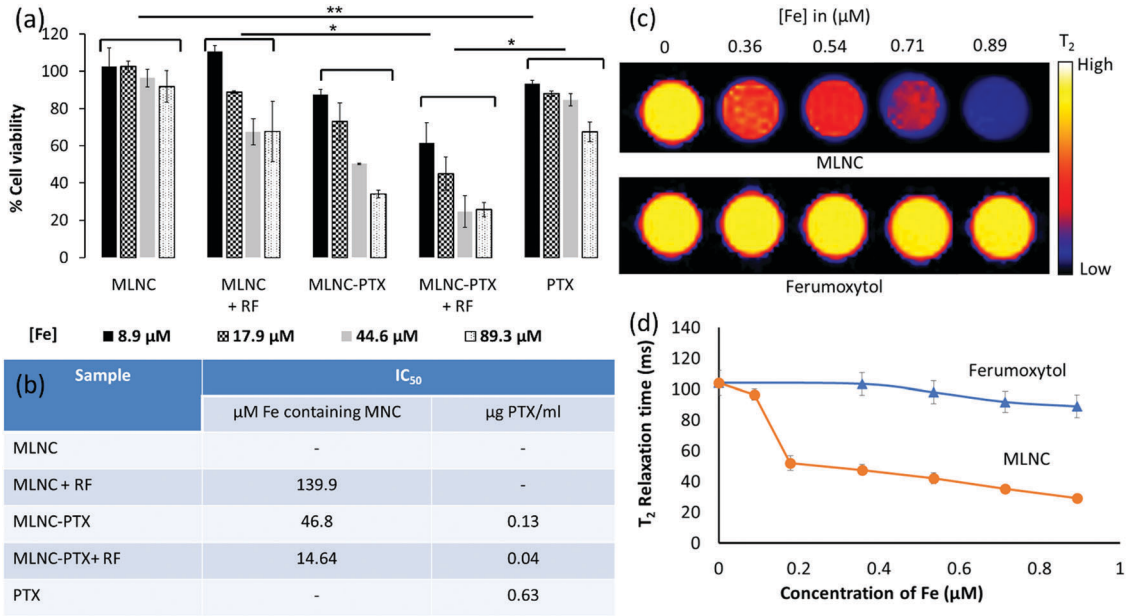

(b)

Sample	IC_{50}	
	μM Fe containing MNC	μg PTX/ml
MLNC	-	-
MLNC + RF	139.9	-
MLNC-PTX	46.8	0.13
MLNC-PTX+ RF	14.64	0.04
PTX	-	0.63

Fig. 5 (a) Cytotoxicity study of HepG2 cancer cells when treated by combination therapy or single treatments with different concentrations of MLNCs with/without PTX and with/without the application of RF field. Cell viability was assessed 24 h after treatment. Significance (**$p < 0.001$, *$p < 0.05$) was calculated by one-way ANOVA using GraphPad Prism 5.0. (b) IC_{50} values for different treatments of HepG2 cells after 48 h calculated using GraphPad Prism 5.0. (c and d) T_2 weighted phantom MRI images and T_2 relaxation times of HepG2 cell pellets treated with different concentrations of MLNCs using a 7 T Bruker Biospin MRI instrument.

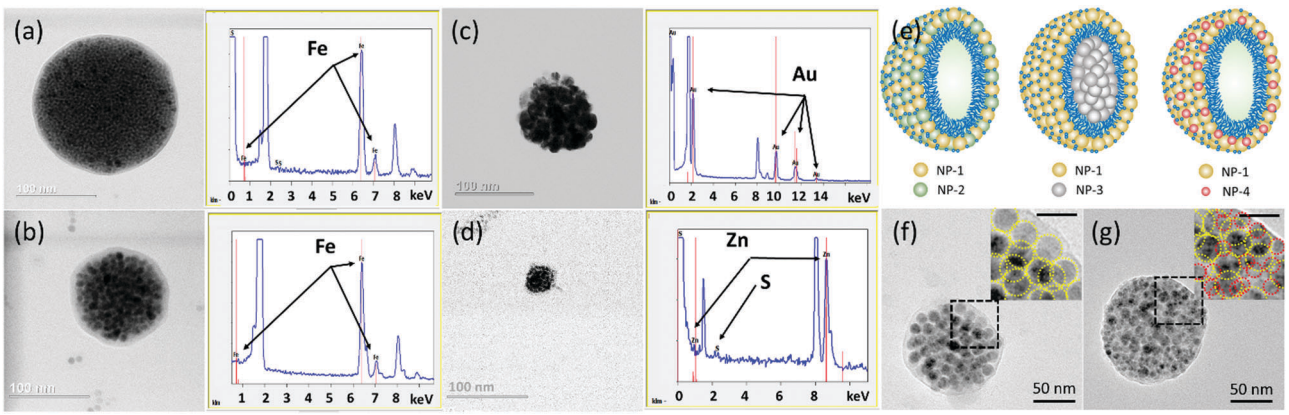

Fig. 6 TEM images and EDX spectra of (a) 180 nm magnetic lipid nanocapsules from 4 nm MNS, (b) 100 nm magnetic lipid nanocapsules from 8 nm MNS, (c) 80 nm plasmonic lipid nanocapsules from 13 nm Au NPs, and (d) 40 nm semiconducting lipid nanocapsules from 6 nm CdSe/ZnS quantum dots. (e) Schematic of multifunctional hybrid nanocapsules using nanoparticles with distinct sizes and/or functionalities encapsulated and/or embedded in the lipid layer. (f) MLNCs with 18 nm MNS. (g) MLNCs with 18 and 8 nm MNS.

are shown in Fig. S7 (ESI†). Nanoparticle assembly results in collective physical properties;[55–57] therefore, the physical properties of nanocapsules can be further tuned by tuning their sizes. However, it should be noted that the clinical translation of Au NPs and QDs has been a challenge due to their persistence in organisms after their designed action.[58] We also demonstrate that the synthetic method can be used to fabricate hybrid structures by integrating different nanoparticles with distinct sizes and/or functionalities. MLNCs were prepared with 18 nm MNSs only (Fig. 6f) and with 18 and 8 nm MNSs (Fig. 6g). Due to its simple and versatile nature, this synthetic method can be used to fabricate multifunctional hybrid structures using a combination of nanoparticles encapsulated and/or integrated on the surface with tunable physical properties (Fig. 6e).

In conclusion, we report MNS-stabilized lipid-based theranostic nanoconstructs, termed MLNCs. The presence of MNS in the MLNCs contributes to structural stability, diagnostic imaging, and thermo/chemo therapy. From a diagnostic perspective, the contrast enhancement of the MLNCs is 8.5 times higher than that of ferumoxytol, an FDA-approved T_2 MRI contrast agent. From a therapeutic perspective, in addition to actuated drug release ability, the MLNCs show higher payload capacity

[drug : lipid ratio up to 0.4 (w/w)] for lipophilic drugs than most clinically approved lipid-based nanocarriers. This results in an IC_{50} value 16 times lower than that of free drug for HepG2 cells. The ability to image with high signal-to-noise ratio, high therapeutic efficacy and high structural stability compared to conventional lipid-based carriers makes the MLNCs an ideal lipid-based theranostic platform in biomedicine. When coupled with the desired targeting agents, these next-generation lipid-based nanocarriers will have great potential in targeted theranostic applications.

Experimental

Synthesis of citrate or amine MNS

$Zn_{0.2}Mn_{0.8}Fe_2O_4$ nanoparticles were used as magnetic cores of MNS and were synthesized using a previously reported thermal decomposition method.[59–61] The as-synthesized oleic acid-coated hydrophobic $Zn_{0.2}Mn_{0.8}Fe_2O_4$ nanoparticles were functionalized with citrate or dopamine *via* a ligand exchange process, resulting in negatively or positively charged MNS.[60] The particle diameters and size distributions of the MLNCs were determined from TEM and DLS. The final concentration of Fe in MNS was determined by ICP-MS analysis.

Synthesis of magnetic lipid nanocapsules (MLNCs)

The MLNCs were synthesized by mixing citrate MNS and a cationic lipid (DDAB or DOTAP) at a particular MNS : lipid ratio. In a typical synthesis, 10 μL aqueous dispersion of citrate MNS (1–4 mg mL^{-1} Fe), 10 μL chloroform dispersion of DDAB (5–25 mg mL^{-1}), and 480 μL Milli-q water were emulsified for 30 s and left overnight at room temperature for self-assembly. The mixture was centrifuged to remove MNS that did not participate in assembly formation and dialyzed to remove any residual surfactants and lipids using a dialysis bag (MWCO = 10 000) for 2 d in water. A 200 nm syringe filter was used to remove any precipitates and the final concentrations of Fe and other metals in the MLNCs were determined by ICP-MS analysis. The MLNCs demonstrated high colloidal stability across a wide pH range buffers and cell culture media.

Drug encapsulation

To prepare drug-loaded MLNCs, a stock solution was first prepared by mixing equal volumes of cationic lipid (5–25 mg mL^{-1}) and drug (0.05–0.5 mg mL^{-1}; CUR or PTX) in chloroform. The same procedure used to synthesize the MLNCs was used except that instead of the cationic lipid solution, the cationic lipid + drug stock solution was used. Finally, the drug-loaded MLNCs were dialyzed using a dialysis bag (MWCO = 10 000) for 2 d in water. The dispersion was then centrifuged to remove drugs that were not encapsulated within the MLNCs. The amount of drug entrapped within the MLNCs was measured by fluorescence (for CUR) or HPLC (for PTX). The drug encapsulation efficiency was calculated as (final drug concentration/initial drug concentration) × 100. For CUR, CUR-loaded MLNCs were measured under fluorescence at an excitation wavelength of 500 nm and an emission range of 525 to 700 nm. For HPLC measurement, PTX-loaded MLNCs were diluted five times with acetonitrile and sonicated in a water bath sonicator for 1 min to extract the drug from the MLNCs and dissolve the drug in acetonitrile. The MLNCs were then centrifuged for 10 min at 13 800 rpm and 10 °C. The supernatants were removed to estimate the amount of entrapped PTX using HPLC. Samples (200 μl) were injected using an autosampler and analyzed using acetonitrile : water (80 : 20 v/v) as the mobile phase at a flow rate of 1 mL min^{-1} using an Agilent HPLC-1100 system. The amount of PTX was quantified by a diode array detector at 228 nm. The amount of drug (PTX) in the sample was determined from the peak area *via* correlation with the standard curve. The HPLC results suggested that 1 μg of PTX was entrapped within MLNCs containing 357.2 μM Fe.

Drug release

Thermal activation/drug release experiments were performed on an MSI Automation Inc. Hyperthermia Research System RF generator at a frequency of 300 kHz and a power of 7 kW. A 0.2 mL suspension was placed inside the 5 cm coil to generate an AC magnetic field of 5 kA m^{-1}. A nonmagnetic nonmetallic optical temperature probe (Fiso) was used to monitor the temperature. The duration of each experiment was 15 min. Released drug was separated by centrifugation, and the fluorescence of the supernatant was measured to calculate the amount of released drug.

Structural characterization

Particle size measurements and energy-dispersive X-ray spectroscopy (EDX) were conducted on Hitachi H8100 TEM (200 kV) and Hitachi HD2300 (200 kV) instruments. The hydrodynamic diameter and zeta potential of the MLNCs were measured using a Malvern Zeta Sizer Nano S-90 dynamic light scattering (DLS) instrument.

Measurement of r_2 relaxivity

The samples (MLNCs, citrate MNS, and Ferumoxytol®) were diluted to metal ion concentrations ranging from 0.01 to 0.3 mM. The T_2 relaxation times were determined at 3.0 T on a Magnetom Verio system (Siemens Healthcare, Erlangen, Germany) using the multiple-echo-fast-spin-echo sequence (TR = 1290 ms, 8 echo times from 9.9 to 79.2 ms, 160 mm FOV, 256 × 256 matrix, slice thickness = 3 mm). Because we had multiple samples with a distribution of T_2 relaxation times, the echo time range may not have been optimal for every sample. A commercial 12-channel head coil (diameter ~160 mm) was used. A 1.5 mL Eppendorf centrifuge tube was used as the sample holder. R_2 maps were generated using a custom software program in Matlab. The signal decay was fit to a single exponential function to estimate T_2 on a pixel-by-pixel basis.

Cell culture

The HepG2 liver cancer cell line and J774 murine macrophage cells (kindly provided by Prof. Colby Shad Thaxton, Department of Urology, Feinberg School of Medicine, Northwestern University) were grown in RPMI-1640 medium containing 10% FBS and penicillin/streptomycin (100 units per mL and 100 μg per mL, respectively).

The cells were cultured at 37 °C with 5% CO_2 atmosphere in T75 flasks.

MTS assay for cell viability tests

The biocompatibility of the void MLNCs was tested in J774 and HepG2 cells using MTS [3-(4,5-dimethylthiazol-2-yl)-5-(3-carboxymethoxyphenyl)-2-(4-sulfophenyl)-2*H*-tetrazolium] assay. Briefly, the cells were plated at 1×10^5 cells per well in a 24-well plate with 70–80% confluency. To study biocompatibility, J774 and HepG2 cells were incubated with MLNCs without drug at [Fe] ranging from 9, 18, 45 μM for 24 h at 37 °C. After 24 h, cells were treated with MTS reagent for 2 h at 37 °C. MTS assay was used to quantify the cell viability according to the protocol provided by the manufacturer (CellTiter 96 Aqueous One Solution Cell Proliferation Assay; Promega). The optical densities were recorded at 490 and 700 nm using a BioTek Synergy™ 4 Hybrid Microplate Reader. The background absorbance at 700 nm was subtracted from the absorbance at 490 nm. The percentages of cell viability for different treatments were calculated in relation to the control samples (cells without out any treatment kept under the same conditions were considered to be 100% viable).

To study cytotoxicity, HepG2 cells were incubated with MLNCs or drug-loaded MLNCs at [Fe] ranging from 9, 18, 45 μM for 24 h at 37 °C. To compare the effects of drug-loaded MLNCs and native drug, cells were also treated with different concentrations of native drug (similar to amounts of drug entrapped within the MLNCs as calculated from the HPCL measurements). After 24 h of treatment, the cells were trypsinized and washed, and specified cells were exposed to thermal activation for 20 min and then again reseeded in the 24-well plate. After 24 h, the cells were treated with MTS reagent for 2 h at 37 °C. MTS assay was used to quantify the cell viability as described earlier. The IC_{50} values were calculated by fitting to a nonlinear curve using the dose response–inhibition equation in GraphPad Prism 5.0. The combination index was calculated using the following formula: combination index = $[CI_1]/I_1 + [CI_2]/I_2$, where $[CI_1]$ is the concentration of therapy1 in combined treatment to induce IC_{50}, $[CI_2]$ is the concentration of therapy2 in combined treatment to induce IC_{50}, $[I_1]$ is the concentration of therapy1 to induce IC_{50} individually, and $[I_2]$ is the concentration of therapy2 to induce IC_{50} individually.

Quantitative analysis of cellular uptake pattern

HepG2 cells were plated at 4×10^6 cells per well in a T25 flask with 70–80% of confluency one day prior to particle treatment. The cells were then cultured with MLNCs at [Fe] 0.9 to 36 μM for 24 h. Untreated cells were used as the control. The cells were washed with DPBS, and ICP-MS was used to quantify the Fe content in the cells. For each sample, 2 μL was removed and used to quantify the total protein content. For ICP-MS, cells were digested using 3% nitric acid overnight and processed the next day (iCapQ ICP-MS, Billerica, Thermo Fischer Scientific). The amounts of Fe in the cell samples were represented as μg Fe per μg protein sample.

Transmission electron microscopy of cell pellets

Cellular uptake and localization of MLNCs in the cells were observed by TEM/EDS of HepG2 cells (4×10^6 cells in a T25 flask) incubated with MLNCs at [Fe] 1 μg mL^{-1} for 4 h. After incubation, the cells were collected and fixed with a mixture containing 2.5% glutaraldehyde and 2% formaldehyde. Post-fixation was conducted with osmium tetroxide. After dehydration using a series of ethanol washes, the sample was embedded in resin. Ultramicrotome sections were placed on TEM grids, and images were collected along with EDS spectra.

In vitro MRI

4×10^6 HepG2 cells were plated in a T25 flask with 70–80% confluency one day prior to particle treatment. The cells were cultured at various concentrations (0.005, 0.1, 0.2, 0.3, 0.4 and 0.5 μg Fe containing MLNCs per mL) for 4 h. Untreated cells were used as the control. Cell pellets were collected and placed in capillaries, which were then closed at both the ends. After arrangement, the cell pellets were imaged using a 7 T Bruker Biospin MRI (Bruker Biospin, Billerica, MA). The images were processed using Paravision 6.0 software.

Conflicts of interest

There are no conflicts to declare.

Acknowledgements

V. N., A. S., and V. P. D. gratefully acknowledge support from the NTU-NU Institute for NanoMedicine located at the International Institute for Nanotechnology, Northwestern University, USA and the Nanyang Technological University, Singapore. This work made use of the EPIC, Keck-II, and/or SPID facility(ies) of Northwestern University's NUANCE Center, which has received support from the Soft and Hybrid Nanotechnology Experimental (SHyNE) Resource (NSF ECCS-1542205); the MRSEC program (NSF DMR-1121262) at the Materials Research Center; the International Institute for Nanotechnology (IIN); the Keck Foundation; and the State of Illinois, through the IIN.

References

1 T. M. Allen and P. R. Cullis, *Adv. Drug Delivery Rev.*, 2013, **65**, 36–48.
2 H. Xing, K. Hwang and Y. Lu, *Theranostics*, 2016, **6**, 1336–1352.
3 S. Mura, D. T. Bui, P. Couvreur and J. Nicolas, *J. Controlled Release*, 2015, **208**, 25–41.
4 J. M. Caster, A. N. Patel, T. Zhang and A. Wang, *Wiley Interdiscip. Rev.: Nanomed. Nanobiotechnol.*, 2017, **9**, e1416.
5 S. Mura, J. Nicolas and P. Couvreur, *Nat. Mater.*, 2013, **12**, 991–1003.
6 L. Sercombe, T. Veerati, F. Moheimani, S. Y. Wu, A. K. Sood and S. Hua, *Front. Pharmacol.*, 2015, **6**, 286.
7 L. F. Zhang and S. Granick, *Nano Lett.*, 2006, **6**, 694–698.
8 S. J. Soenen, G. Vande Velde, A. Ketkar-Atre, U. Himmelreich and M. De Cuyper, *Wiley Interdiscip. Rev.: Nanomed. Nanobiotechnol.*, 2011, **3**, 197–211.

9 G. V. Orsinger, S. J. Leung, S. S. Knights-Mitchell, J. D. Williams and M. Romanowski, Nanotechnology, *Technical Proceedings of the 2012 NSTI Nanotechnology Conference and Expo, NSTI-Nanotech 2012*, 2012, 134–137.
10 C. J. Wen, C. T. Sung, I. A. Aljuffali, Y. J. Huang and J. Y. Fang, *Nanotechnology*, 2013, **24**, 325101.
11 D. Yoo, J. H. Lee, T. H. Shin and J. Cheon, *Acc. Chem. Res.*, 2011, **44**, 863–874.
12 J. Kim, Y. Piao and T. Hyeon, *Chem. Soc. Rev.*, 2009, **38**, 372–390.
13 N. Lee and T. Hyeon, *Chem. Soc. Rev.*, 2012, **41**, 2575–2589.
14 N. Lee, D. Yoo, D. Ling, M. H. Cho, T. Hyeon and J. Cheon, *Chem. Rev.*, 2015, **115**, 10637–10689.
15 L. H. Reddy, J. L. Arias, J. Nicolas and P. Couvreur, *Chem. Rev.*, 2012, **112**, 5818–5878.
16 V. Nandwana, M. De, S. Chu, M. Jaiswal, M. Rotz, T. J. Meade and V. P. Dravid, in *Cancer treatment and research*, ed. C. A. Mirkin, T. J. Meade, S. Hurst Petrosko and A. H. Stegh, ch. Theranostic Magnetic Nanostructures (MNS) for Cancer, 2015, vol. 166, pp. 51–83.
17 M. R. Prince, H. L. Zhang, S. G. Chabra, P. Jacobs and Y. Wang, *J. X-Ray Sci. Technol.*, 2003, **11**, 231–240.
18 Y. Kono, R. F. Mattrey, S. C. Rose, T. Hassanein and K. Hart, *Hepatology*, 1999, **30**, 278A.
19 R. Sharma, S. Saini, P. R. Ros, P. F. Hahn, W. C. Small, E. E. de Lange, A. E. Stillman, R. R. Edelman, V. M. Runge, E. K. Outwater, M. Morris and N. Lucas, *Chin. J. Magn. Reson. Imaging*, 1999, **9**, 291–294.
20 M. De, S. S. Chou, H. M. Joshi and V. P. Dravid, *Adv. Drug Delivery Rev.*, 2011, **63**, 1282–1299.
21 H. Fattahi, S. Laurent, F. J. Liu, N. Arsalani, L. V. Elst and R. N. Muller, *Nanomedicine*, 2011, **6**, 529–544.
22 B. Garnier, S. Tan, S. Miraux, E. Bled and A. R. Brisson, *Contrast Media Mol. Imaging*, 2012, **7**, 231–239.
23 O. Bixner and E. Reimhult, *J. Colloid Interface Sci.*, 2016, **466**, 62–71.
24 S. V. German, N. A. Navolokin, N. R. Kuznetsova, V. V. Zuev, O. A. Inozemtseva, A. A. Anis'kov, E. K. Volkova, A. B. Bucharskaya, G. N. Maslyakova, R. F. Fakhrullin, G. S. Terentyuk, E. L. Vodovozova and D. A. Gorin, *Colloids Surf., B*, 2015, **135**, 109–115.
25 R. Di Corato, G. Bealle, J. Kolosnjaj-Tabi, A. Espinosa, O. Clement, A. K. A. Silva, C. Menager and C. Wilhelm, *ACS Nano*, 2015, **9**, 2904–2916.
26 D. Frascione, C. Diwoky, G. Almer, P. Opriessnig, C. Vonach, K. Gradauer, G. Leitinger, H. Mangge, R. Stollberger and R. Prassl, *Int. J. Nanomed.*, 2012, **7**, 2349–2359.
27 E. Amstad, J. Kohlbrecher, E. Muller, T. Schweizer, M. Textor and E. Reimhult, *Nano Lett.*, 2011, **11**, 1664–1670.
28 A. Skouras, S. Mourtas, E. Markoutsa, M. C. De Goltstein, C. Wallon, S. Catoen and S. G. Antimisiaris, *J. Nanomed. Nanotechnol.*, 2011, **7**, 572–579.
29 N. Ding, Y. Lu, R. J. Lee, C. Yang, L. Huang, J. Liu and G. Y. Xiang, *Int. J. Nanomed.*, 2011, **6**, 2513–2520.
30 K. G. Victor, J. P. Korb and R. G. Bryant, *J. Phys. Chem. B*, 2013, **117**, 12475–12478.
31 J. Estelrich, M. J. Sanchez-Martin and M. A. Busquets, *Int. J. Nanomed.*, 2015, **10**, 1727–1741.
32 C. Bonnaud, C. A. Monnier, D. Demurtas, C. Jud, D. Vanhecke, X. Montet, R. Hovius, M. Lattuada, B. Rothen-Rutishauser and A. Petri-Fink, *ACS Nano*, 2014, **8**, 3451–3460.
33 A. Floris, A. Ardu, A. Musinu, G. Piccaluga, A. M. Fadda, C. Sinico and C. Cannas, *Soft Matter*, 2011, **7**, 6239–6247.
34 Y. J. Chen, A. Bose and G. D. Bothun, *ACS Nano*, 2010, **4**, 3215–3221.
35 T. Bollhorst, K. Rezwan and M. Maas, *Chem. Soc. Rev.*, 2017, **46**, 2091–2126.
36 X. C. Yang, B. Samanta, S. S. Agasti, Y. Jeong, Z. J. Zhu, S. Rana, O. R. Miranda and V. M. Rotello, *Angew. Chem., Int. Ed.*, 2011, **50**, 477–481.
37 J. E. Park, D. R. Hickey, S. Jun, S. Kang, X. Hu, X. J. Chen and S. J. Park, *Adv. Funct. Mater.*, 2016, **26**, 7791–7798.
38 J. Q. Zhuang, H. M. Wu, Y. G. Yang and Y. C. Cao, *Angew. Chem., Int. Ed.*, 2008, **47**, 2208–2212.
39 S. H. Koenig and K. E. Kellar, *Magn. Reson. Med.*, 1995, **34**, 227–233.
40 A. Roch, Y. Gossuin, R. N. Muller and P. Gillis, *J. Magn. Magn. Mater.*, 2005, **293**, 532–539.
41 C. Paquet, H. W. de Haan, D. M. Leek, H. Y. Lin, B. Xiang, G. H. Tian, A. Kell and B. Simard, *ACS Nano*, 2011, **5**, 3104–3112.
42 S. Laurent, D. Forge, M. Port, A. Roch, C. Robic, L. V. Elst and R. N. Muller, *Chem. Rev.*, 2008, **108**, 2064–2110.
43 K. C. Barick, M. Aslam, P. V. Prasad, V. P. Dravid and D. Bahadur, *J. Magn. Magn. Mater.*, 2009, **321**, 1529–1532.
44 A. N. Tuan, D. T. Quan, C. T. D. Duc and C. D. Mau, *Adv. Nat. Sci.: Nanosci. Nanotechnol.*, 2016, **7**, 035003.
45 M. Mahmud, A. Piwoni, N. Filiczak, M. Janicka and J. Gubernator, *PLoS One*, 2016, **11**, e0173728.
46 I. Jelezova, E. Drakalska, D. Momekova, N. Shalimova, G. Momekov, S. Konstantinov, S. Rangelov and S. Pispas, *Eur. J. Pharm. Sci.*, 2015, **78**, 67–78.
47 U. Bulbake, S. Doppalapudi, N. Kommineni and W. Khan, *Pharmaceutics*, 2017, **9**, 12.
48 S. Kalepu and V. Nekkanti, *Acta Pharmacol. Sin.*, 2015, **5**, 442–453.
49 A. J. ten Tije, J. Verweij, W. J. Loos and A. Sparreboom, *Clin. Pharmacokinet.*, 2003, **42**, 665–685.
50 C. R. Thomas, D. P. Ferris, J. H. Lee, E. Choi, M. H. Cho, E. S. Kim, J. F. Stoddart, J. S. Shin, J. Cheon and J. I. Zink, *J. Am. Chem. Soc.*, 2010, **132**, 10623–10625.
51 S. Purushotham and R. V. Ramanujan, *Acta Biomater.*, 2010, **6**, 502–510.
52 M. K. Jaiswal, M. De, S. S. Chou, S. Vasavada, R. Bleher, P. V. Prasad, D. Bahadur and V. P. Dravid, *ACS Appl. Mater. Interfaces*, 2014, **6**, 6237–6247.
53 E. L. Jones, J. R. Oleson, L. R. Prosnitz, T. V. Samulski, Z. Vujaskovic, D. H. Yu, L. L. Sanders and M. W. Dewhirst, *J. Clin. Oncol.*, 2005, **23**, 3079–3085.
54 P. Wust, U. Gneveckow, M. Johannsen, D. Bohmer, T. Henkel, F. Kahmann, J. Sehouli, R. Felix, J. Ricke and A. Jordan, *Int. J. Hyperthermia*, 2006, **22**, 673–685.

55 M. A. Boles, M. Engel and D. V. Talapin, *Chem. Rev.*, 2016, **116**, 11220–11289.
56 S. Gwo, H. Y. Chen, M. H. Lin, L. Y. Sun and X. Q. Li, *Chem. Soc. Rev.*, 2016, **45**, 5672–5716.
57 Z. D. Lu and Y. D. Yin, *Chem. Soc. Rev.*, 2012, **41**, 6874–6887.
58 S. P.-M. D. Cassano and V. Voliani, *Bioconjugate Chem.*, 2017, DOI: 10.1021/acs.bioconjchem.7b00664.
59 V. Nandwana, K. E. Elkins, N. Poudyal, G. S. Chaubey, K. Yano and J. P. Liu, *J. Phys. Chem. C*, 2007, **111**, 4185–4189.
60 V. Nandwana, S. R. Ryoo, S. Kanthala, M. De, S. S. Chou, P. V. Prasad and V. P. Dravid, *ACS Appl. Mater. Interfaces*, 2016, **8**, 6953–6961.
61 V. Nandwana, S. R. Ryoo, S. Kanthala, K. M. McMahon, J. S. Rink, Y. Li, S. S. Venkatraman, C. S. Thaxton and V. P. Dravid, *Chem. Mater.*, 2017, **29**, 2276–2282.